Initiation and Propagation of Compaction Bands in Dry and Wet Bentheim Sandstone

SERGEI STANCHITS,[1] JEROME FORTIN,[2] YVES GUEGUEN,[2] and GEORG DRESEN[1]

Abstract—We investigated initiation and propagation of compaction bands (CB) in six wet and four dry Bentheim sandstone samples deformed in axial compression tests with strain rates ranging from 3.2×10^{-8} s^{-1} to 3.2×10^{-4} s^{-1}. Circumferential notches with 0.8-mm width and 5-mm depth served to initiate CB at mid-sample length. Wet samples were saturated with distilled water and deformed at 195 MPa confining pressure and 10 MPa pore pressure. Dry samples were deformed at 185 MPa confining pressure. Twelve P-wave sensors, eight S-wave sensors and two pairs of orthogonally oriented strain-gages were glued to the sample surface to monitor acoustic emission (AE), velocities and local strain during the loading process. Nucleation of compaction bands is indicated by AE clusters close to the notch tips. With progressive loading, AE activity increased and AE hypocenters indicated propagation of a single CB normal to the sample axis. CB propagation from the sample periphery towards the centre was monitored. Microstructural analysis of deformed samples shows excellent agreement between location of AE clusters and CBs. In both dry and wet samples the lateral propagation of CBs was about 100 times faster than axial shortening rates. At the slowest displacement rate, AE activity during band propagation was reduced and CB nucleation in wet samples occurred at 20% lower stresses. This may indicate an increasing contribution of stress corrosion processes to the formation of the compaction bands. In dry and wet samples inelastic compaction energy per area ranged between 16 and 80 kJ m^{-2}. This is in good agreement with previous estimates from laboratory and field studies.

Key words: Compaction bands, acoustic emission, fracture, rock.

1. Introduction

Localized compaction bands in high porosity rocks are narrow zones with significantly reduced local porosity. MOLLEMA and ANTONELLINI (1996) described the existence of CBs in the Navajo sandstone formation of southern Utah (USA). STERNOF et al. (2005) observed CB arrays in Aztec sandstone exposed in the southeastern part of Nevada (USA). Inside the CBs, porosity is only a few percent and significantly reduced with respect to the initial 20–25% porosity of the sandstone.

[1] GeoForschungsZentrum Potsdam, Department 3.2, Telegrafenberg D420, 14473 Potsdam, Germany. E-mail: stanch@gfz-potsdam.de

[2] Laboratoire de Geologie, Ecole Normale Superieure, CNRS, UMR 8538, 24 rue Lhomond, 75005 Paris, France. E-mail: fortin@geologie.ens.fr

Compaction bands may form permeability barriers affecting fluid circulation and extraction of oil and gas from reservoirs, and may have important implications for the management of both groundwater and hydrocarbon resources (TAYLOR and POLLARD, 2000; STERNLOF *et al*., 2004 and 2006). Recent laboratory studies have demonstrated that compaction localization is an important failure mode in different sandstones with porosities ranging from 13 to 28% (OLSSON and HOLCOMB, 2000; DIGIOVANNI *et al*., 2000; KLEIN *et al*., 2001; WONG *et al*., 2001; BAUD *et al*., 2004, 2006, FORTIN *et al*., 2005). FORTIN *et al*. (2006) analyzed the AE hypocenter distribution in order to investigate CB propagation in Bleurswiller sandstone. They found a close spatial correspondence of AE clusters and CB observed in the deformed samples.

Some field observations suggest development of compaction bands induced by local stress concentrations. For example, MOLLEMA and ANTONELLINI (1996), observed formation of compaction bands in the compressional quadrant close to the tip of a shear band. In laboratory tests on sandstone specimens, nucleation of CBs was found to occur at boreholes or notches. Haimson and co-workers (HAIMSON 2001, 2003; KLAETSCH and HAIMSON, 2002; HAIMSON and KOVACHICH, 2003; HAIMSON and LEE, 2004) in true-triaxial tests of porous sandstones observed the formation of slot-like borehole breakouts that are very similar to compaction bands.

VAJDOVA and WONG (2003) investigated formation of CBs in Bentheim sandstone samples with a circumferential V-shaped notch. They observed propagation of CBs from the notch tip in sequential increments. CB formation was accompanied by bursts of AE activity and reduction of axial force applied to the sample. TEMBE *et al*. (2006) report CB initiation in sandstones with porosities ranging from 21% to 23% subjected to confining pressures between 150 MPa and 350 MPa. These authors found a close correspondence of experimental results with a spring network model presented by KATSMAN and AHARONOV (2006), which simulates local compactive failure by shortening the bond length. The model of KATSMAN and AHARONOV (2006) shows that discrete compaction bands could be nucleated at the notch tip and propagate incrementally through the entire sample cross section, similar to experimental observations. In the spring-network model the shortening of the bonds is also accompanied by a local stress drop.

The energy required to develop compaction bands was estimated to range from 6 to 43 kJ m^{-2} (VAJDOVA and WONG, 2003; TEMBE *et al*., 2006). This is more than 1000 times higher than the specific surface energy (of the order of 1 J m^{-2}) of tensile fractures of minerals (ATKINSON and MEREDITH, 1987), yet comparable to shear fracture energies for rocks under triaxial compression (WONG, 1982; LOCKNER *et al*., 1991). TEMBE *et al*. (2006) suggested that micromechanisms involved in the formation of compaction and shear bands are similar (intense microcracking and grain crushing), leading to dissipation of significant amounts of inelastic energy. The energy estimates based on laboratory tests are in a good agreement with field observations (about 40 kJ m^{-2}, STERNLOF *et al*., 2005), and with energies predicted from mechanical models (RUDNICKI and STERNLOF, 2005; RUDNICKI, 2007). RUDNICKI (2007) recently presented an anti-crack-dislocation model of CB propagation. The model predicts the band thickness (or midpoint closure) to increase

with the square root of the band half-length, assuming that energy release rate of CB propagation remains constant. This theoretical prediction is in good agreement with the results of field observations (MOLLEMA and ANTONELLINI, 1996; STERNLOF et al., 2005).

VAJDOVA and WONG (2003) identified three stages of CB formation in notched Bentheim sandstone: (a) Nucleation of a compaction band, (b) extension of a diffuse compaction band, and (c) development of an array of compaction bands. AE activity suggested that growth of CBs occurred in increments and is roughly 100 times faster than axial shortening of the samples. Brittle faulting of low-porosity rock has been thoroughly studied in the laboratory during the last two decades using AE hypocenter localization (LOCKNER, 1993; LEI et al., 1992, 2000; ZANG et al., 1998, 2000; THOMPSON et al., 2006; STANCHITS et al., 2006). It has been demonstrated that AE data provide important constraints for the analysis of the onset of shear localization. In a recent paper FORTIN et al. (2006) successfully applied AE hypocenter analysis and showed a close spatial agreement between the position of individual CBs and the corresponding AE hypocenter clusters. In this study we use a similar technique to monitor geometrical and AE characteristics and energy dissipation during CB propagation in dry and wet Bentheim sandstone.

2. Experimental Techniques

2.1. Sample Material and Testing Procedure

Experiments were performed on cylindrical samples of 50 mm diameter and 105 mm length cored from Bentheim sandstone (Gildehaus quarry, Germany). Bentheim sandstone (BS) is a Lower Cretaceous, homogeneous, yellow sandstone, containing 95% quartz, 3% feldspar, and 2% kaolinite (KLEIN and REUSCHLE, 2003). Porosity of BS is about 22%, grain size varies from 18 μm to 500 μm and the mean grain size is about 300 μm (REINICKE et al., 2008). Specimens were prepared with a circumferential notch at mid-sample length. The notch is 0.8 mm wide with a depth of 5 mm (Fig. 1). A teflon O-ring of about 0.7 mm thickness was used to fill the notch to prevent rupture of the Neoprene jacket used to insulate samples from the oil confining medium. Experiments were performed on dry and wet Bentheim samples. Dry samples were kept in an oven at 50°C temperature under vacuum ($\sim 10^{-2}$ bar) for at least 12 hours. After jacketing and installation in the pressure vessel the samples were subjected to a vacuum of $\sim 10^{-2}$ bar for about 12 hours before loading. The vacuum was maintained during the experiment. To prepare wet samples, specimens were first saturated with distilled water for more than 12 hours. Tests were carried out at drained conditions with a constant pore fluid (water) pressure $P_P = 10$ MPa using a QUIZIX pore pressure pump.

For all tests, effective confining pressure was maintained constant at $P_{\text{eff}} = (P_C - P_P) = 185$ MPa, where P_C and P_P are confining pressure and pore pressure, respectively. Experiments were performed at constant displacement rate in a servo-hydraulic loading frame from Material Testing Systems (MTS) with a load capacity of 4600 KN. Strain
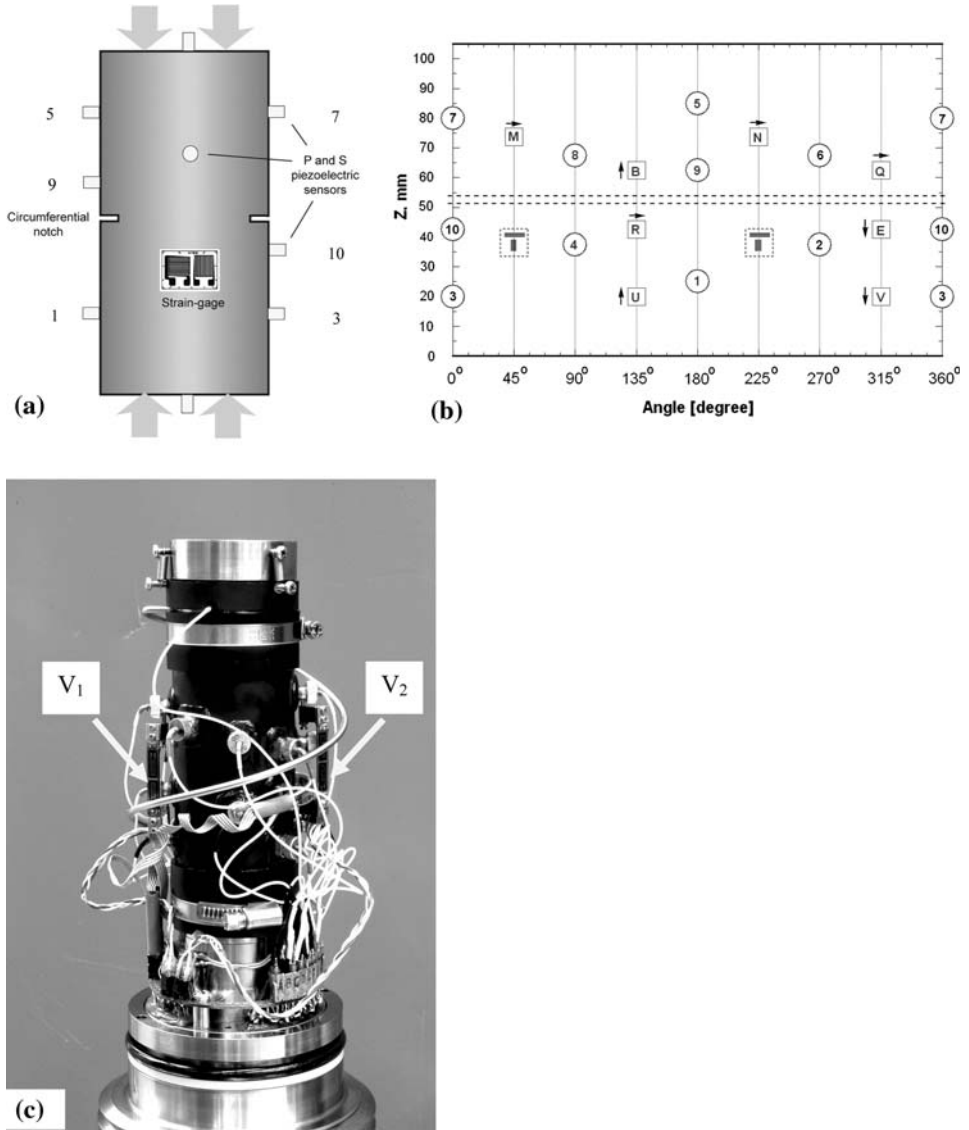
Figure 1
(a) Sketch of notched sample; (b) projected sample surface showing position of *P*-piezoelectric sensors (circles), *S* sensors (squares) and strain-gages (dashed-squares). Arrows indicate direction of *S*-sensors polarization; (c) photo of sample assembly. Vertical extensometers, measuring shortening between upper and lower halves of the sample are marked as V_1 and V_2.

rates were varied between 3.2×10^{-8} s^{-1} and 3.2×10^{-4} s^{-1}. Axial load was measured with an external load cell with an accuracy of 1 kN corrected for seal friction of the loading piston.

2.2. Strain Measurements and Acoustic Emission (AE) Monitoring

Axial strain ε_{ax} was measured using a linear variable displacement transducer (LVDT) mounted at the end of the loading piston. Data were corrected for the effective stiffness (793 kN/mm) of the loading frame. In addition, two pairs of orthogonally oriented strain gages were glued directly to the specimen surface in axial and circumferential direction (Fig. 1b). Volumetric strain Δ_S was calculated using: $\Delta_S = \varepsilon_1 + 2\varepsilon_3$, where ε_1 and ε_3 are axial and circumferential strain, respectively. For wet specimens the change in pore fluid volume and connected porosity Δ_W was monitored using a volumometer with accuracy of about 0.001 cm^3. Compressive stresses, compactive strains and porosity reduction are considered positive. The maximum and minimum compressive stresses are denoted by σ_1 and σ_3, and the differential stress by $Q = (\sigma_1 - \sigma_3)$.

To monitor AE and ultrasonic velocities, twelve P-wave and eight polarized S-wave sensors were glued directly to the surface of the rock and sealed in the jacket with two-component epoxy (Fig. 1c). Piezoelectric P- and S-wave sensors were fabricated from PZT piezoceramic discs with 5 mm diameter and 2 mm thickness and rectangular piezoceramic plates $5 \times 5 \times 1$ mm, respectively. The thickness and diameter-related resonant frequencies of the P-wave sensors are about 1 MHz and 400 KHz, respectively. Transducer signals were amplified by 40 dB using Physical Acoustic Corporation (PAC) preamplifiers equipped with 100 kHz high-pass filters. To measure P- and S- wave velocities in different sample directions and monitor velocity changes during the loading, some sensors were used periodically for elastic wave emission applying 100 V electrical pulses. Intervals between velocity measurements varied with sample loading rate from 5 to 1000 seconds. Full-waveform AE and ultrasonic signals were stored in a 12- channel transient recording system (DAXBox PRÖKEL, Germany) with an amplitude resolution of 16 bit at 10 MHz sampling rate (STANCHITS *et al.*, 2006). Ultrasonic transmissions and AE waveforms were discriminated automatically after the experiments. During the experiments, all waveforms were recorded in transient memory with no dead time between consecutive signals. During periods of high AE activity signals were recorded continuously.

The AE hypocenters location procedure includes automatic picking of P-wave onset time based on the Akaike information criterion (LEONARD and KENNETT, 1999) and minimization of travel-time residuals using the downhill simplex algorithm (NELDER and MEAD, 1965) considering time-dependent changes of velocities (STANCHITS *et al.*, 2006). The recording system allows locating successfully up to 1000 AE signals per second. We estimate the AE hypocenter location accuracy to be < 2 mm.

3. Experimental Results

3.1. Mechanical Data

In total, ten experiments were performed on notched samples. Six samples were deformed wet and four samples were dry. Based on the analysis of mechanical and AE
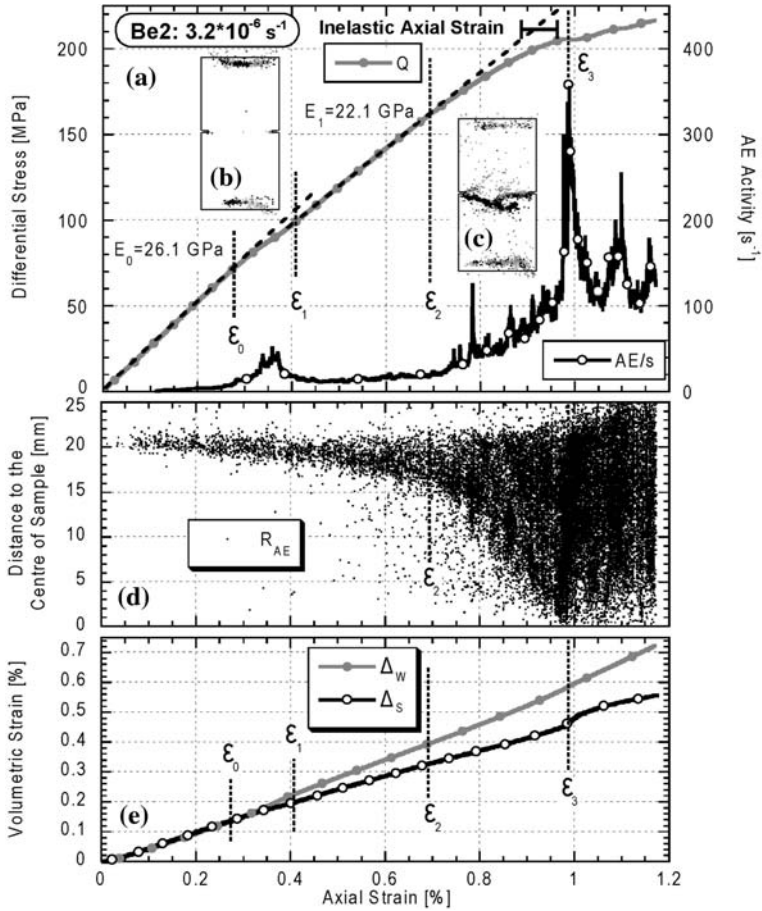
Figure 2

(a) Stress-strain curve and acoustic emission activity registered during deformation of wet sample Be2 with intermediate strain rate 3.2×10^{-6} s^{-1}; (b) AE hypocenters registered during interval of axial deformation ($\varepsilon_0 - \varepsilon_1$); (c) AE hypocenters registered during CB propagation ($\varepsilon_2 - \varepsilon_3$); (d) distance between AE hypocenters in the notched area ($32.5 < Z < 72.5$ mm) and the sample axis ($r = \sqrt{X^2 + Y^2}$;) (e) volumetric strains measured from a change in the pore volume (Δ_W) and by strain gages (Δ_S) versus axial strain.

data, we separate several deformation stages (Fig. 2). The initial part of the loading curve ($\varepsilon_{ax} < \varepsilon_0$) is almost linear (Fig. 2a), and the volumetric strain monitored by strain gages is close to the strain estimated from the change in the pore fluid volume (Fig. 2e). In all experiments we observed the appearance of diffuse AE clusters close to the sample top and bottom. About 13% of AEs registered during this stage were located in the notched area, whereas 87% were located at the top and bottom part of the sample (Fig. 2b). These clusters most likely result from stress concentration due to end-cap friction, beginning at a stress level of 40%–60% of the stress required for CBs initiation at the notch tip. Similar concentration of AE events near the ends of the specimens was observed for other

sandstone and loading conditions in FORTIN *et al.* (this issue). With progressive loading the Young's modulus decreases (Fig. 2a). At axial strain $\varepsilon_{ax} > \varepsilon_1$, the volumetric strains Δ_W and Δ_S diverge (Fig. 2e). The change in pore fluid volume Δ_W is a representative measure for the entire specimen, as opposed Δ_S from the strain gages, which represent local measurements of areas of about 10 mm^2 below the gage.

CB nucleation is characterized by the onset of AE activity near the notch tip, and the nonlinear shape of the loading curve (Fig. 2a). At CB nucleation about 72% of AE hypocenters are located at the notched area of the sample, indicating to the propagation of CB through the entire crosssection (Fig. 2c). For each AE event we calculated the distance (R_{AE}) of AE hypocenter (X, Y) to the center of sample as $R_{AE} = \sqrt{X^2 + Y^2}$. Propagation of the AE front starting from the notch tip (Fig. 2d) towards the specimen center coincides with an increase of AE activity (Fig. 2a). Propagation of the CB front is not uniform, but involves emission of episodic AE bursts (Figs. 2a, 2d), probably indicating individual increments of CB propagation.

Young's moduli from all experiments from different loading stages are given in Table 1. We separate elastic Δ_{El}, ε_{ax_El} and inelastic Δ_{Inel}, $\varepsilon_{ax\_Inel.}$ volumetric and axial strain, respectively, assuming that $\Delta_{Tot} = \Delta_{El} + \Delta_{Inel}$ and $\varepsilon_{ax\_Inel.} = \varepsilon_{ax} - \varepsilon_{ax\_El}$ (SCHOLZ, 1968; Fig. 3b). The cumulative AE number registered in the central part of the sample

Table 1

Summary of experimental results. E_0 and E_1 —Young's modules registered during two elastic stages of loading; ε_1 and ε_2 —axial strain at the moments of CB initiation and completion, respectively; Q_1 and Q_2 — differential stress at the moments of CB initiation and completion, respectively; h_{CB} — compactive shortening across the band determined as the slope of curves Figure 14; E_{AE_Eff} and W_{CB} — cumulative effective AE energy and dissipated inelastic mechanical energy, respectively, at the moment of CB completion; last three columns — energy release densities determined by different techniques: G_{CB} — from mechanical data according to equation (5); G_{CB_AC} — according to anti-crack model of RUDNICKI and STERNLOF (2005) by equation (6); G_{K1} — using K_1 according to TEMBE et al. (2006) by equation (8)

Wet Samples

Sample	Strain Rate	E_0, GPa	E_1, GPa	ε_1,%	ε_2,%	Q_1, MPa	Q_2, MPa	h_{CB}, mm	W_{CB}, J	E_{AE_Eff}, V^2 s	G_{CB}, kJ/m^2	G_{CB_AC}, kJ/m^2	G_{K1}, kJ/m^2
Be4	3.2×10^{-8}	24.7	22.5	0.59	0.76	132	156	0.073	30.5	0.86	24.3	23.3	16.0
Be11	3.2×10^{-7}	24.8	20.7	0.66	0.90	148	179	0.107	25.0	0.76	19.9	35.6	20.0
Be2	3.2×10^{-6}	26.1	22.3	0.75	0.99	173	205	0.148	62.1	2.09	49.4	52.9	26.1
Be10	3.2×10^{-5}	27.1	17.5	0.79	0.99	183	210	0.094	27.2	3.06	21.7	34.6	28.1
Be17	1×10^{-5}	26.6	18.7	0.77	0.97	171	197	0.076	20.3	2.08	16.2	31.9	24.9
Be3	3.2×10^{-4}	26.2	19.8	0.81	0.98	176	198	0.089	34.2	4.53	27.2	32.2	27.2

Dry Samples

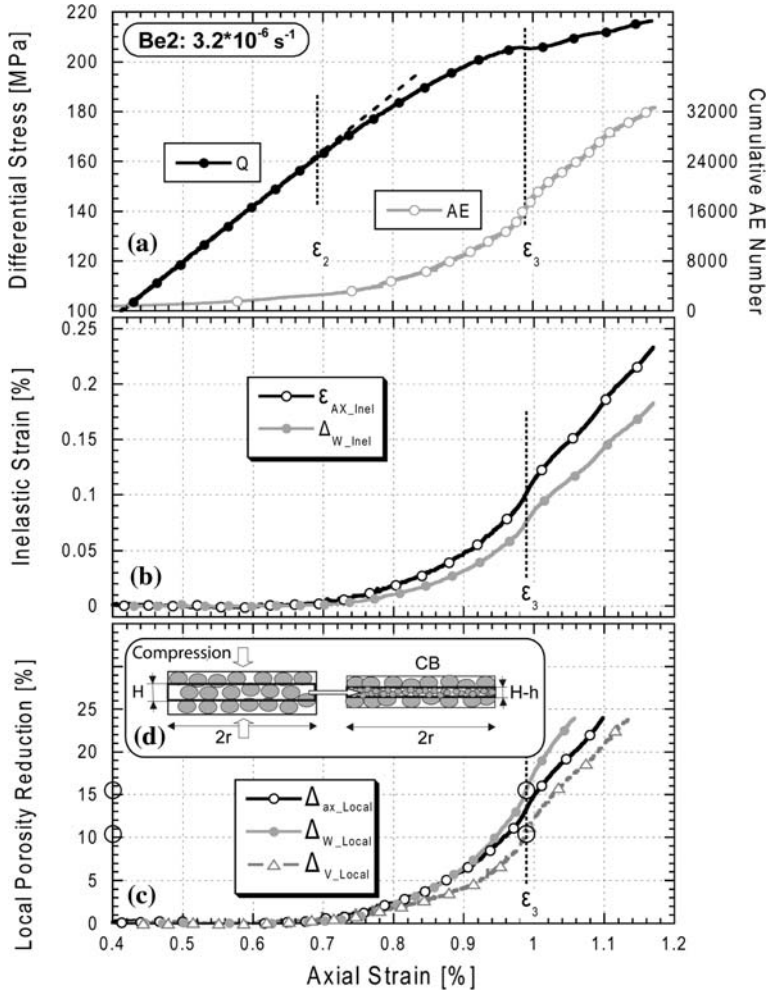| Sample	Strain Rate	E_0, GPa	E_1, GPa	ε_1, %	ε_2, %	Q_1, MPa	Q_2, MPa	h_{CB}, mm	W_{CB}, J	E_{AE_Eff}, V^2 s	G_{CB}, kJ/m^2	G_{CB_AC}, kJ/m^2	G_{K1}, kJ/m^2
Be15	3.2×10^{-8}	26.6	22.8	0.71	1.0	168	201	0.228	100	4.56	79.6	82.6	24.1
Be14	3.2×10^{-6}	23.9	21.1	0.66	0.92	147	179	0.111	63.1	8.66	50.3	38.8	20.4
Be6	3.2×10^{-5}	25.8	22.6	0.67	0.84	149	176	0.075	39.8	13.9	31.7	23.7	19.7
Be19	3.2×10^{-4}	25.8	22.0	0.62	0.92	134	181	0.104	38.9	15.0	31.0	63.5	16.0

Figure 3

(a) Loading curve and cumulative AE number registered during deformation of wet sample Be2 at intermediate strain rate 3.2×10^{-6} s^{-1} versus axial strain; (b) inelastic axial and volumetric strains; (c) Local porosity reduction estimated by three independent measuring techniques, assuming that deformation of notched sample is localized in the notched area (radius $r = 20$ mm and height $H_{CB} = 0.8$ mm); (d) synoptic picture indicating CB formation adopted from KATSMAN and AHARONOV (2006).

corresponds closely to the increase of the inelastic axial strain (Figs. 3a, b). Inelastic axial strain ε_{ax_Inel} monitored by axial shortening of the sample and inelastic volumetric strain Δ_{W_Inel} estimated independently from a change in the pore fluid volume are very similar during CB propagation stage $\varepsilon_2 < \varepsilon_{ax} < \varepsilon_3$. Assuming that sample deformation is localized in the notched area having radius $r = 20$ mm and height $H_{CB} = 0.8$ mm (equal to the notch width), we can roughly estimate local inelastic porosity reduction from ε_{ax_Inel} and Δ_{W_Inel} (Fig. 3c). For comparison we also included results, obtained from
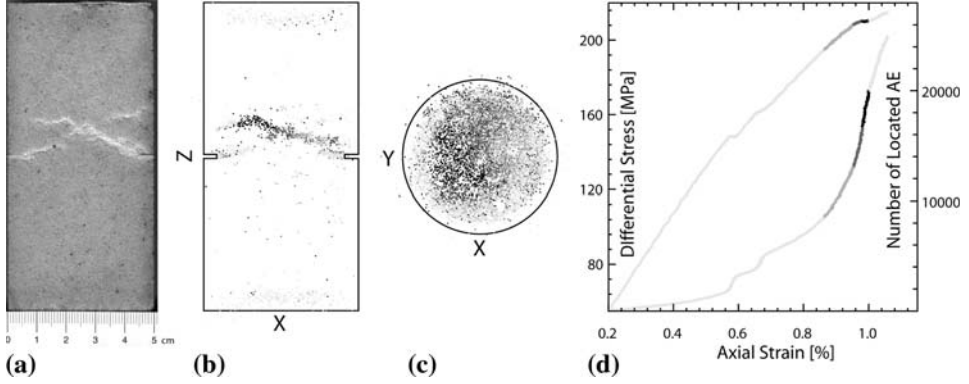
Figure 4

(a) Photo of deformed sample Be10 (strain rate 3.2×10^{-5} s^{-1}, wet conditions). Light areas in the photo (Fig. 4a) correspond to highly damaged areas of sandstone, or CBs; (b) hypocenter locations of acoustic emission events in (X−Z) plane between Y = −1.5 mm and Y = +1.5 mm, selected with AE adjusted amplitude higher than 2 Volts (we determined AdjAmp according to ZANG *et al.* (1998), as amplitude adjusted for geometrical spreading of AE); (c) hypocenter locations of acoustic emission events in (X−Y) plane between Z = 32.5 mm and Z = 72.5 mm; (d) loading history and cumulative AE number versus axial strain. Gray color code corresponds to the time sequences of AE events appearance: lighter color — earlier events, darker color — closest to the completion of CB events. To highlight stage of CB propagation, AEs registered after CB completion are marked by light color.

vertical extensometers, Δ_{V_Local} (marked as V_1 and V_2 in Fig. 1c), directly measuring shortening between upper and lower parts of the sample. From these measurements we conclude that during CB propagation radial strain is negligibly small (Fig. 3c). At CB completion, (ε_3 in Fig. 3c), local porosity reduction Δ_{Inel_Local} inside the CB obtained by three independent techniques ranges from 10.4%–15.5%.

3.2. Analysis of AE Hypocenters and CB Propagation

In all experiments discrete compaction bands nucleated at the notch tip and propagated towards the center of the specimen covering the entire crosssection. Loading was stopped after completion of compaction band propagation. After the experiment, the samples were cut in two halves parallel to the long sample axis and the maximum compressive stress direction. Locations of AE hypocenters and trace of CB on cut through the sample are in good agreement indicating high location accuracy (Figs. 4a, 4b). This suggests that the uncertainty in hypocenter location for high amplitude AEs is possibly < 1 mm, as it has been observed in our previous study (FORTIN *et al.*, 2006).

Analysis of AE hypocenter locations allows monitoring of CB nucleation and propagation (Figs. 5, 6). Usually CB propagation towards the center of the specimens follows a corrugated path, in agreement with microstructural observations (see section 3.3, Figs. 10, 11). In general, CB propagation involves coalescence of individual defect clusters, finally resulting in complex through-going and curved bands slightly
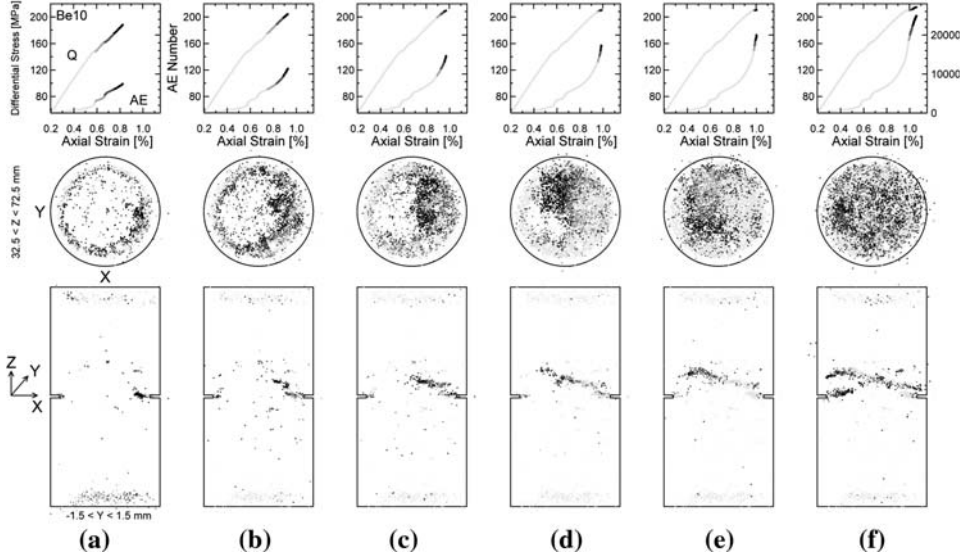
Figure 5

Compaction band initiation and propagation in sample Be10 during loading at intermediate strain rate $(3.2 \times 10^{-5} \text{ s}^{-1})$ at wet conditions. In the lower and middle rows two projections of cumulative hypocenter distributions are shown, divided by 6 time sequences (a)–(f). For the middle row, demonstrating X−Y projection, we selected AE events from the central part of the sample at 20 mm distance to the notch $(32.5 < Z < 72.5 \text{ mm})$. For the lower row we selected AE events located in the same (Z−X) plane as shown in Figure 4b $(-1.5 < Y <+ 1.5 \text{ mm})$. Upper row plots show dependence of differential stress and cumulative AE number versus axial strain. Gray color code is the same for all three rows, demonstrating time sequences of AE events appearance for each snap-shot (a)–(f): lighter color — earlier events, darker color — most recent events. In total in experiment Be10 we have successfully located about 25000 AE events.

inclined to the plane of the circumferential notch (Figs. 5, 6). Completion of compaction band propagation is associated with a small stress drop in the loading curve (Fig. 5e, 6e), similar mechanical characteristics were observed by VAJDOVA and WONG (2003) and TEMBE *et al.* (2006). After compaction band completion we can see some branching and a reduced AE activity (Figs. 5f, 6f).

AE hypocenter locations, onset of inelastic deformation, P-wave velocities, and abrupt increase in AE activity all indicate CB nucleation and reveal the evolution of individual bands (Fig. 7, 8). To define CB nucleation we investigated the spatial distribution of AE, calculating the correlation integral (HIRATA *et al.*, 1987):

$$C(R) = \frac{2}{N(N-1)} N_{(r < R)}, \tag{1}$$

where $N_{(r < R)}$ is the number of AE hypocenter pairs separated by a distance smaller than R. $C(R)$ is a measure for the degree of clustering and localization varying between 0 and 1. For $R \to \infty$, $C(R) = 1$ and for $R = 0$, $C(R) = 0$. Correlation coefficient
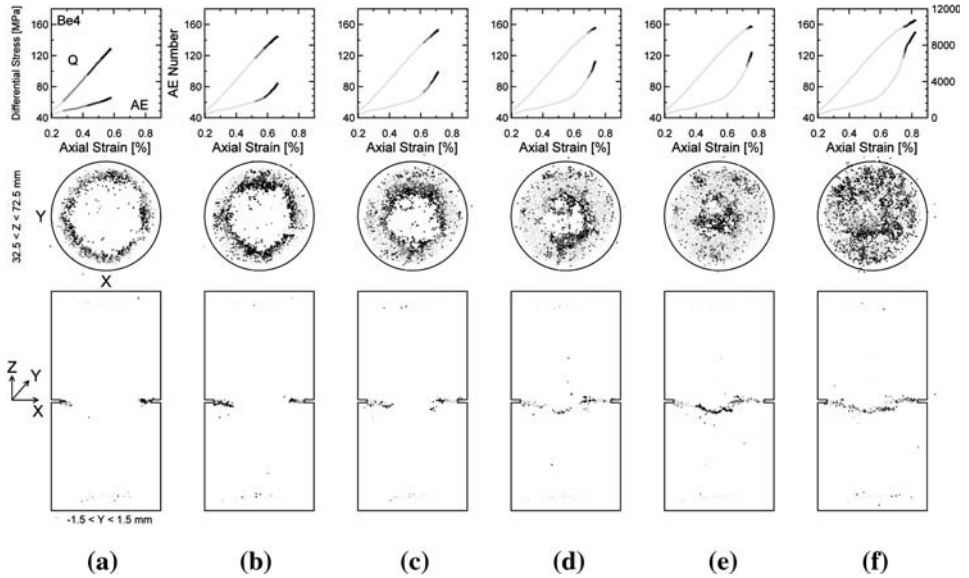
Figure 6

Time sequences of compaction band initiation and propagation in sample Be4 — slowest strain rate (3.2×10^{-8} s^{-1}, wet conditions). Figure captions are the same as in Figure 5. In total in experiment Be4 we have successfully located about 10000 AE events.

(C value) is calculated by (1) for $R = 1$ cm (ZANG *et al.*, 1996). Drastic increase of C value indicates CB nucleation coinciding with the increase in AE activity (Figs. 7c, 7d and 8c, 8d).

   P-wave velocities help identifying completion of the CB (Fig. 7e, 8e). As shown by FORTIN *et al.* (2006) elastic wave velocities decrease during formation of compaction bands. This is explained by the nucleation of new cracks involved in the process of compaction localization. In our experimental setup, *P*-wave velocities along ray paths outside and across the CB were recorded. Close to the moment of CB completion *P*-wave velocities along ray paths outside and across the CB start to significantly diverge. The velocity of ultrasonic signals crossing single CB decreases by almost 1% (Figs. 7e, 8e). In addition, AE magnitudes and AE activity (Figs. 7c, 8c) decrease after the CB reached the specimen centre.

   The cross-section area covered by AE is estimated from (X−Y) projection of AE hypocenter distribution of events with adjusted amplitude more than 3 V that exceed a critical density varying between samples in the range 2.5–13.5 AE events/mm^2. Adjusted amplitude is calculated for a distance of 10 mm from the AE hypocenter assuming geometrical spreading of elastic waves (LOCKNER *et al.*, 1992; ZANG *et al.*, 1998). The cross-section area defined in this way shows an increase with axial strain (Figs. 7b, 8b), that corresponds closely to the increase in inelastic axial strain.
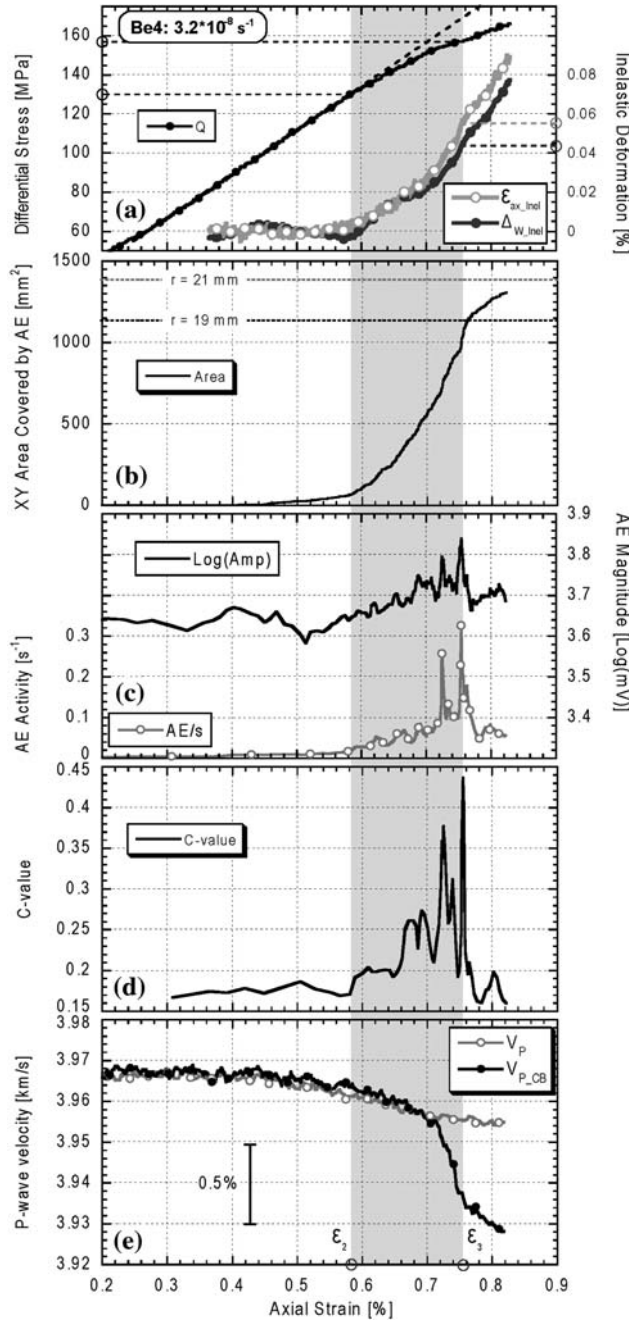
◄

Figure 7

Parameters indicating initiation and completion of compaction bands in experiment Be4 (slowest strain rate, wet conditions) versus strain rate. (a) Differential stress (Q), inelastic axial strain (opened circles) and inelastic volumetric strain (filled circles) measured by pore pressure pump volumometer; (b) CB area calculated from AE hypocenter distribution analysis; (c) AE activity (opened circles) and logarithm of adjusted AE amplitude (solid line); (d) correlation coefficient calculated by equation (1) for $R = 1$ cm; (e) P-wave velocity measured outside of notched area (opened circles) and crossing notched area along ultrasonic transmission trace (9)–(10) (solid circles).

3.3. Microstructural Analysis of CB

After the tests, samples were unloaded and impregnated with blue epoxy. Optical thin sections (30 μm thickness) were prepared from the notched part of the samples. We analyzed wet samples deformed at the fastest (Be3) and the slowest (Be4) loading rates by optical microscopy at GFZ Potsdam and by scanning electron microscopy (SEM) at ENS Paris. The photo mosaics of Figure 9a reveal that starting from the notch the CBs are zones of intense grain damage and reduced porosity, following an angular path through the specimen. Inside the bands, grains are crushed and fragments fill up the collapsed pore space (Figs. 9, 10). Regardless of the applied loading rate, the reduced porosity inside the bands is in the range of 10–15%, as determined by SEM picture analysis. Outside the band, the rock matrix remains mostly undeformed with a porosity of about 24%.

From SEM pictures, we determined the damage zones (Figs. 11a, 12a). The comparison with the AE hypocenter locations reveals close spatial agreement (Fig. 11). Analysis of SEM micrographs for the slowest loading rate (Fig. 11) gives a total CB length, $L_{CB} = 47.6$ mm and the damaged area, $S_{CB} \sim 37.8$ mm^2. For the fastest loading rate (Fig. 12), CB length and damage area are $L_{CB} = 55.6$ mm and $S_{CB} = 51.7$ mm, respectively. However, we found slightly higher mean width of CB in the fastest experiment Be3 ($H_{CB} = 0.92$ mm) compared to the slowest experiment Be4 ($H_{CB} = 0.8$ mm). Note that in both cases, the thicknesses of the compaction bands are close to the thickness of the notch (0.8 mm).

4. Discussion

4.1. Rate Dependence of Stress Required to Initiate CB and Propagation Velocity

Differential stress Q, and axial strain ε_{ax}, at the nucleation and completion of the CBs increases slightly for samples deformed in the presence of a pore fluid, but remains about constant for dry samples (Figs. 13a, 13b). We refer to completion of a CB once the entire sample diameter is covered with located AE hypocenters. In wet samples, the stress needed to initiate CB is strain rate sensitive, and increases with increasing strain rate. Similar results were reported for the stress needed to initiate shear localization in creep experiments performed on Darley Dale sandstone by Baud
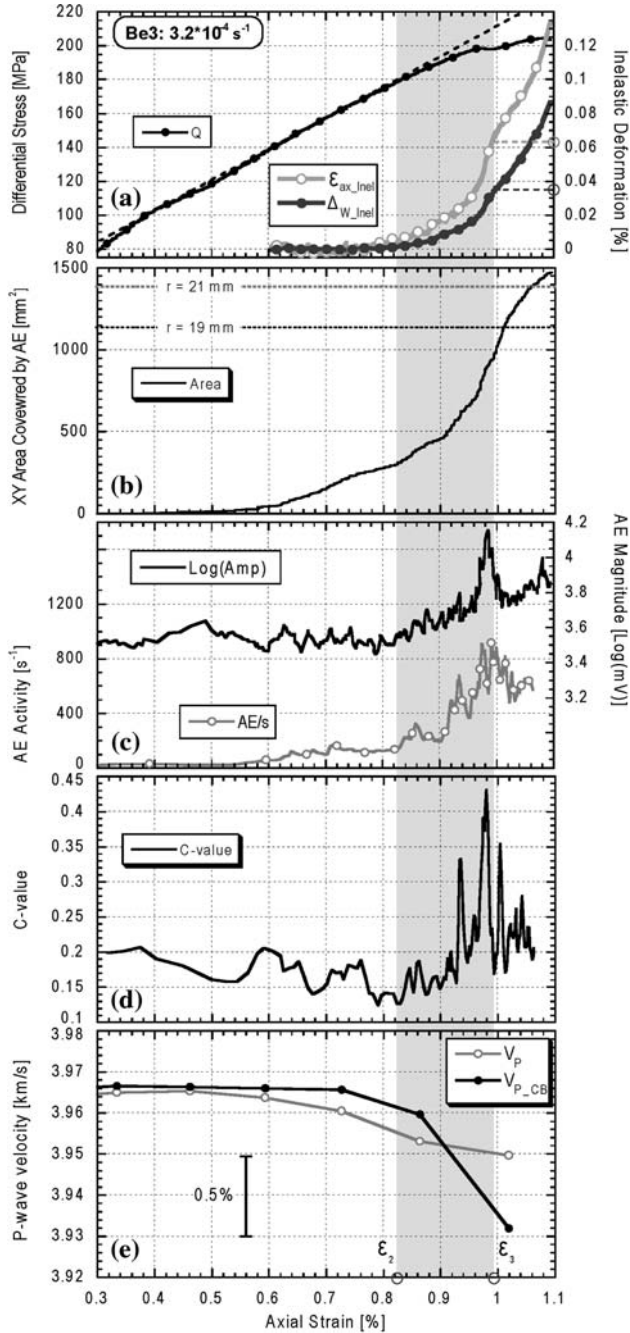
Figure 8
Parameters indicating initiation and completion of compaction bands in experiment Be3 (fastest strain rate, wet conditions) versus strain rate. Figure captions are the same as for Figure 7.
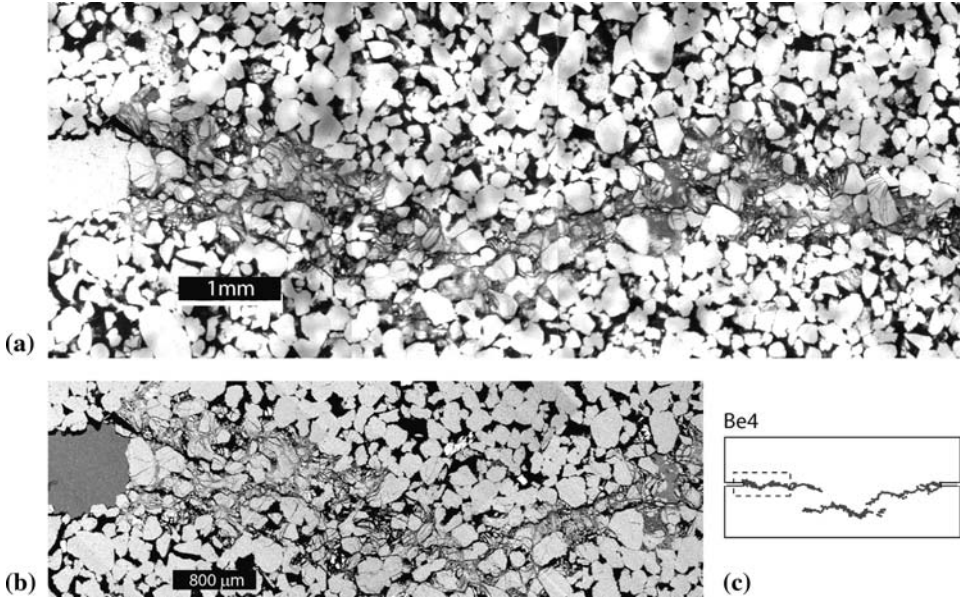
Figure 9

(a) Optical and (b) SEM microphotos (backscattered electron image) of sample Be4 thin section (slowest strain rate 3.2×10^{-8} s^{-1}, wet conditions); (c) dash rectangle indicates position of taken microphotos on the Be4 sample map.

and Meredith (1997). It is conceivable that the loading rate dependence of CB formation of wet samples may be related to stress corrosion processes contributing significantly to sample compaction at the lowest rates (ATKINSON and MEREDITH, 1981). This explanation is confirmed by the results obtained for dry samples. In dry samples, no strain rate dependence for the stress at the onset of CB is observed (Fig. 13c). The stress corrosion process is time-dependent and should depend on the stress field because the chemical activity of the pore fluid is affected by pressure. Similar influence of strain rate on the strength of dry and wet Tennessee sandstone was reported by RUTTER and MAINPRICE (1978).

Irrespective of the loading rate, the total axial strain required to propagate individual CBs across the sample diameter (axial strain at completion minus axial strain at initiation) remains roughly constant between about 0.1–0.3% (Figs. 13b, 13d) corresponding to vertical displacements between 0.1–0.3 mm. The radial distance from the notch tip to the specimen center is 20 mm. This indicates that the propagation velocity of the CB tip across the sample is approximately a factor of 100 faster than the axial shortening velocity perpendicular to the band in agreement with observations of VAJDOVA and WONG (2003), and TEMBE et al. (2006). This ratio remains almost constant over about four orders of magnitude shortening rates for wet and dry samples (Fig. 13).

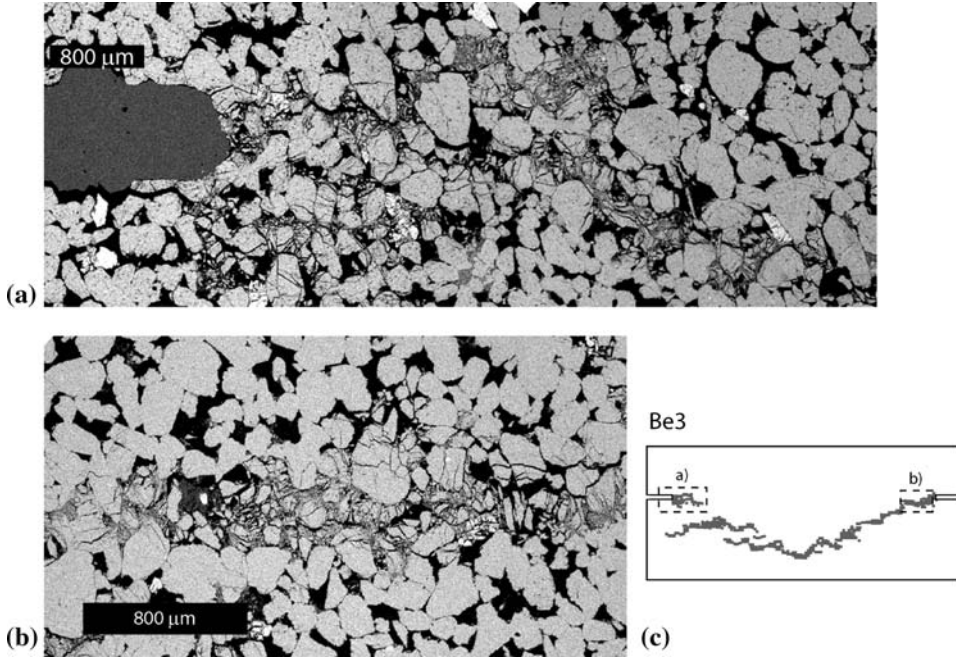Figure 10
(a), (b) SEM microphotos (backscattered electron image) of sample Be3 thin section (fastest strain rate 3.2×10^{-4} s^{-1}, wet conditions). (c) Dash rectangles indicate positions of taken microphotos on the Be3 sample map.
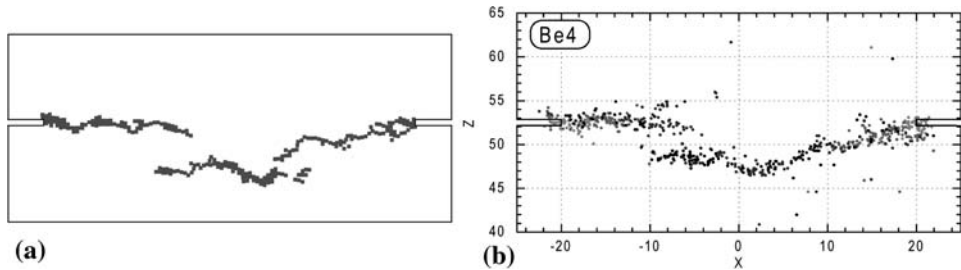

Figure 11
Comparison of damage zones obtained by SEM microstructural analysis (a) and AE hypocenter locations (b) of sample Be4 (slowest strain rate 3.2×10^{-8} s^{-1}, wet conditions).

4.2. Compaction Band Shortening during CB Propagation

The inelastic component of the axial strain of the sample increases during propagation of CB towards the sample center (Fig. 3b). Inelastic axial strain monitored by strain gages and inelastic volumetric strain monitored by the volumometer are almost identical within error of the measurements (Fig. 3b). This indicates that the radial component of
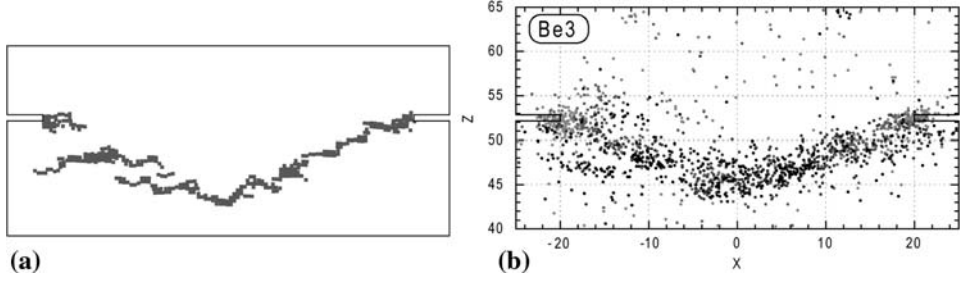
Figure 12

Comparison of damage zones obtained by SEM microstructural analysis (a) and AE hypocenter locations (b) of sample Be3 (fastest strain rate 3.2×10^{-4} s^{-1}, wet conditions).
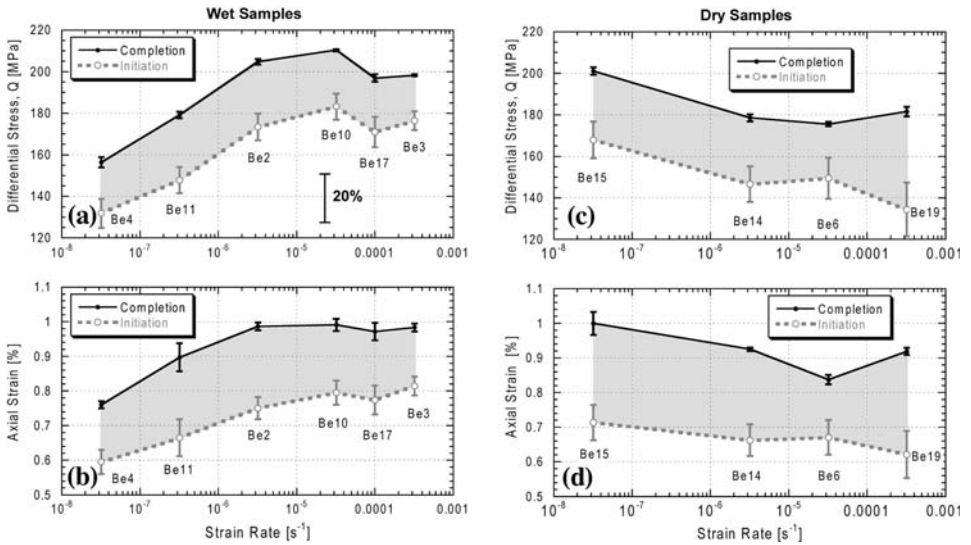

Figure 13

Differential stress (a), (c) and axial strain (b), (d) versus strain rate for wet (a), (b) and dry (c), (d) experiments. Error bars presented in the figure indicate accuracy of moments of CB initiation (gray color) and completion (black color) estimation. They are calculated for each experiment as maximal and minimal values determined by combination of different mechanical, ultrasonic and AE criteria.

the plastic strain is zero and that compaction only involves axial shortening. Consequently, the slope of the change in plastic volumetric strain and plastic shortening with change in area covered by the compaction band are measures for the compactive shortening across the band (h_{CB}):

$$h_{CB} = \frac{\partial(P_{Vol\_Inel})}{\partial(S_{CB})} \cong \frac{\partial(d_{Inel})}{\partial(S_{CB})} * S_N, \qquad (2)$$

where P_{Vol_Inel} is inelastic pore volume reduction, S_{CB} is area covered by AE cloud, d_{Inel} is inelastic displacement and $S_N = \pi r^2$ is area of the notched part of the sample
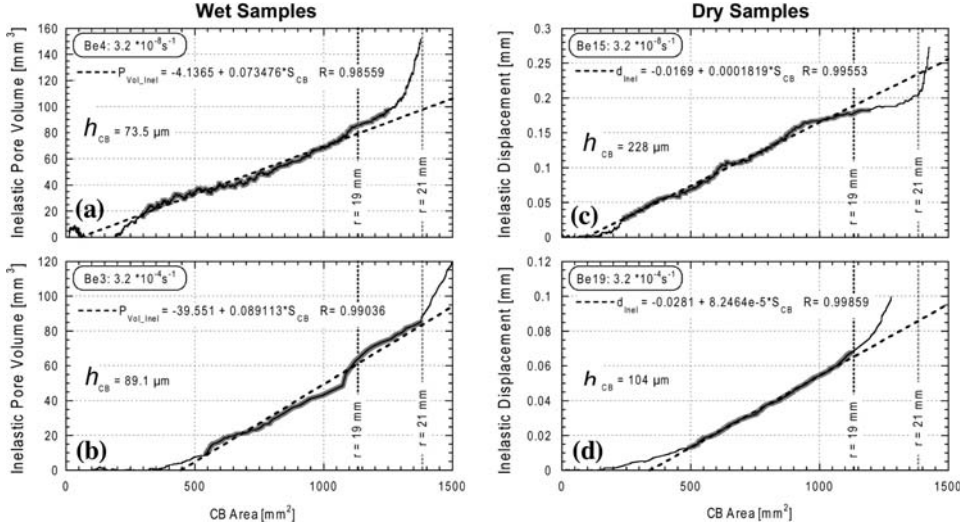
Figure 14

Inelastic pore volume reduction in wet experiments (a), (b) and inelastic displacement in dry experiments (c), (d) versus area covered by AE events. Experiments were performed at slowest (a), (c) and fastest (b), (d) loading rates.

($r = 20$ mm). The data for wet and dry samples indicate a linear relation of inelastic pore volume reduction (Figs. 14a, 14b) and inelastic displacement (Figs. 14c, d) with a change in CB area. The CB shortening h_{CB} remains relatively constant between 70–230 μm during propagation of the band (Table 1). This value is similar to the average grain size in Bentheim sandstone and significantly smaller than the thickness of the notch. From this the local axial and volumetric strain are estimated to be $\sim 10\%$–20% for most samples.

A linear relation between local compaction and CB area was also suggested by KATSMAN and AHARONOV (2006) and KATSMAN *et al.* (2006) using a Spring Network Model (SNM). Our data indicate that CB propagation is a stable process that occurs by episodic increments of unstable compactive events indicated by bursts of AE activity (Figs. 2a, 2d). This is reminiscent of the run–away instabilities suggested in the Katsman – Aharonov model.

4.3. Energy Dissipation during CB Propagation

The total inelastic work per unit volume, dw, done on the sample by the inelastic axial deformation dε_{ax_inel}, is (EDMOND and PATERSON, 1972):

$$dw = Q(d\varepsilon_{ax\_inel}) + P_C d\Delta_{inel}, \tag{3}$$

where $d\Delta_{inel}$ is the increment of inelastic volumetric strain. The total inelastic work per unit volume is then (WONG, 1982):

$$w_{CB} = \int_0^{\varepsilon_{inel\_C}} Q(d\varepsilon_{ax\_inel}) + (P_C - P_P)\Delta_{Vol\_Inel}, \tag{4}$$

where Δ_{Vol_Inel} is inelastic volumetric strain, and ε_{inel_c} is the inelastic strain at completion of the compaction band.

From equation (4), the total dissipated inelastic mechanical energy W during formation of CB can be written as a function of the inelastic sample shortening h_{inel}:

$$W_{CB}(h_{inel}) = \int_0^{h_{inel}} F_{Dif}(dh_{inel}) + (P_C - P_P) * \Omega(h_{inel}), \tag{5}$$

where differential force $F_{Dif} = Q\pi R^2$ and $\Omega(h_{inel})$ is pore volume reduction expected in the notched part of the sample. Neglecting inelastic radial deformation of the notched part of the sample ($\Delta_{Vol\_inel} \approx \varepsilon_{ax\_inel}$), we assume that inelastic pore volume reduction is given by $\Omega(h_{inel}) \approx \pi r^2 h_{inel}$. (R is radius of the sample; r is radius of notched part of the sample). Compactive shortening h_{inel} is measured directly in our experiments as described in Section 4.2. The total energy dissipated during CB formation is in the range of $W_{CB} = 20\text{–}100$ J. The results for different samples are summarized in Table 1. The dissipated energy release rate G_{CB} is in the range 16–80 kJ m^{-2} (Table 1).

For all samples the dissipated mechanical energy is linearly related to CB area as estimated from AE analysis (Fig. 15), with a slope representing G_{CB_AE}. G_{CB_AE} is in the range of 27 to 110 kJ m^{-2} irrespective of pore fluid content and loading rate (Fig. 15).
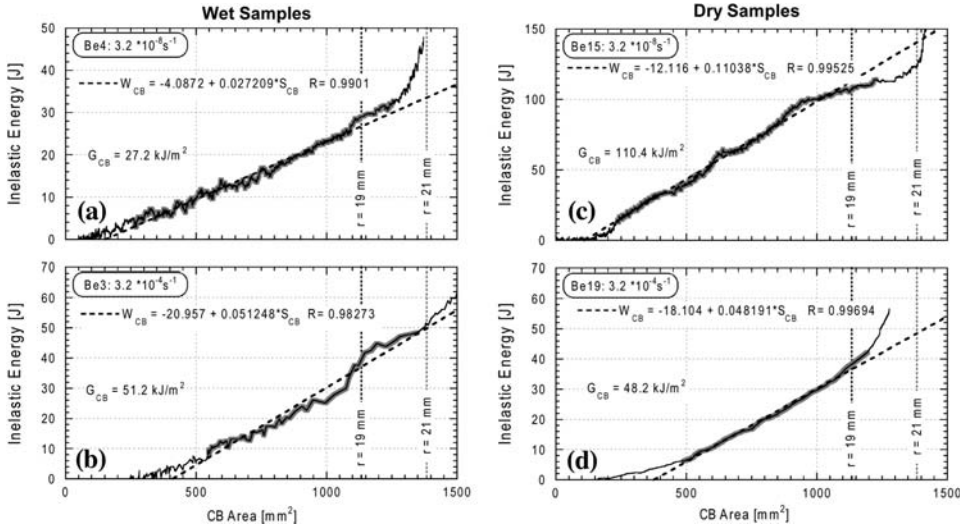

Figure 15
Dissipated inelastic energy versus area covered by AE events in wet (a), (b) and dry (c), (d) experiments performed at slowest (a), (c) and fastest (b), (d) loading rates.

RUDNICKI and STERNLOF (2005) and RUDNICKI (2007) derived an expression for the energy released during CB propagation:

$$G_{CB\_AC} = \sigma_{1*}\zeta h * \varepsilon_p, \tag{6}$$

where σ_1 is uniaxial stress far ahead of the band tip, ε_p is the local plastic compactive strain and ζh is the band thickness. Although the model does not necessarily imply a specific shape of the band or distribution of ε_p, it does assume that the thickness and inelastic strain reach asymptotic values at some lengthy distance behind the tip.

For the specimens investigated in this study, the CB thickness ζh is in the range of 0.8–0.9 mm (Section 3.3, samples Be3, Be4) and ε_p is roughly 0.1. The G_{CB_AC} values for our specimens predicted by the Rudnicki model are in the range 23–83 kJ m^{-2} in good agreement with our experimental measurements G_{CB} (Table 1, Fig. 16). In wet samples, the stress required to initiate CB is strain rate sensitive. Stress increases with rising strain rate, which may indicate a stress corrosion process (Section 5.2, Fig. 13). However, in wet and dry samples the energy release for CB propagation appears to be almost independent of the strain rate within error (Fig. 16).

TEMBE *et al.* (2006) proposed a formulation of the stress intensity factor K_1 for notched cylindrical samples, deformed under uniaxial loading:

$$K_1 = (\sigma_1 - P_C)\sqrt{\pi t}\frac{(1 + 0.5\eta + 0.375\eta^2 - 0.363\eta^3 + 0.731\eta^4)}{2\eta^{3/2}}, \tag{7}$$

where $\eta = r/R$; t is the notch depth ($t = R - r$) and σ_1 the axial stress. Equation (7) shows that K_1 is a function of the notch geometry and the stress state. From our measurements, we estimate the axial stress σ_1 at the moment of CB initiation and calculate a critical stress intensity factor K_{1c} for CB nucleation from equation (7). From K_{1c} the energy release rate may be calculated using the relation (LAWN, 1993):
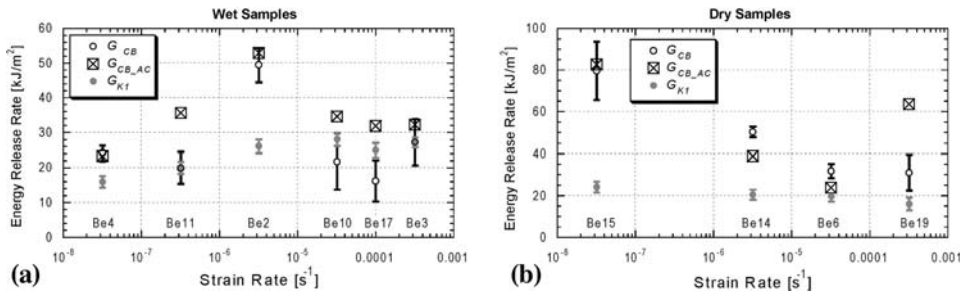

Figure 16

Strain rate dependence of normalized dissipated energy in wet (a) and dry (b) sandstones. Open circles — G_{CB} dissipated inelastic mechanical energy at the CB completion, equation (5); square symbols — G_{CB_AC} critical release rate calculated according to anti-crack model, RUDNICKI and STERNLOF, (2005), equation (6); Gray circles — G_{K1} critical release rate calculated according to equation (8).

$$G_{K1} = \frac{K_{Ic}^2}{E}(1 - v^2),\tag{8}$$

where E is Young's modulus, v is Poisson ratio. Using these relations, we estimated energy release rates G_{KI} for our samples in the range 16–28 kJ m^{-2} (Table 1).

For most wet and dry specimens experimental measurements of G_{CB} and estimates predicted by the models agree within a factor of two (Fig. 16, Table 1). However, for some samples the model predictions G_{CB_AC} and G_{KI} vary by up to a factor of 5, and for all samples G_{KI} is lower than G_{CB_AC} (Table 1). Probably, the calculation of energy release rate G_{KI} using the critical stress intensity factor K_{Ic} (equation 7) underestimates G. For all samples, the experimentally measured energies and those predicted by the models are in the range 16–83 kJ m^{-2} (Table 1) — roughly similar to the results of VAJDOVA and WONG (2003) and TEMBE *et al*. (2006). Based on the field observations of STERNLOF *et al*. (2005), RUDNICKI and STERNLOF (2005) estimate G = 40 kJ m^{-2}. This value is also in the range of our results.

4.4. *Energy Radiated by AE during CB Propagation*

The plastic work W_{CB} done on the sample during formation of CBs is dissipated in the formation of structural defects, as heat, and as kinetic energy radiated as elastic waves or AE. The radiated AE energy E_{AE} is proportional to A^2 where A is the amplitude of the electrical signal registered by the piezoelectric sensors (LOCKNER *et al*., 1991). Our recording system has no rearming time, so AEs could be registered continuously. This allows calculation of the cumulative electrical energy E_{AE} recorded by ten sensors as a proxy for the radiated kinetic energy (ZANG *et al*, (1996)):

$$E_{AE}(N) = \sum_{1}^{N} \sum_{i=1}^{10} \sum_{j=1}^{T} (A_{ij}^2 \Delta t),\tag{9}$$

where A_{jj} is the amplitude registered by sensor i at the sampling time t_j amplified by 40 dB; $\Delta t = 10$ ns is the sampling interval; T is the duration time of a single AE exceeding the voltage threshold (2 V) for at least one channel.

For all experiments during CB formation electrical energy E_{AE} is proportional to dissipated inelastic energy (Fig. 17). Strain rate dependence of radiated electrical energy E_{AE} at the moment of CB completion is shown in Figure 18a, the values are summarized in Table 1. The radiation efficiency ΔE_{AE} (i.e., the ratio of electrical energy E_{AE} and total inelastic energy W_{CB}, Fig. 17) is higher for dry compared to wet samples and it increases with increasing loading rate (Fig. 18b). At slow loading rates, wet and dry samples show similar ΔE_{AE}. This indicates that the observed difference could not be attributed to a difference in attenuation of wet and dry samples. We suggest that at slow loading rates and in wet samples subcritical crack growth contributes more efficiently to compaction and CB formation compared to dry
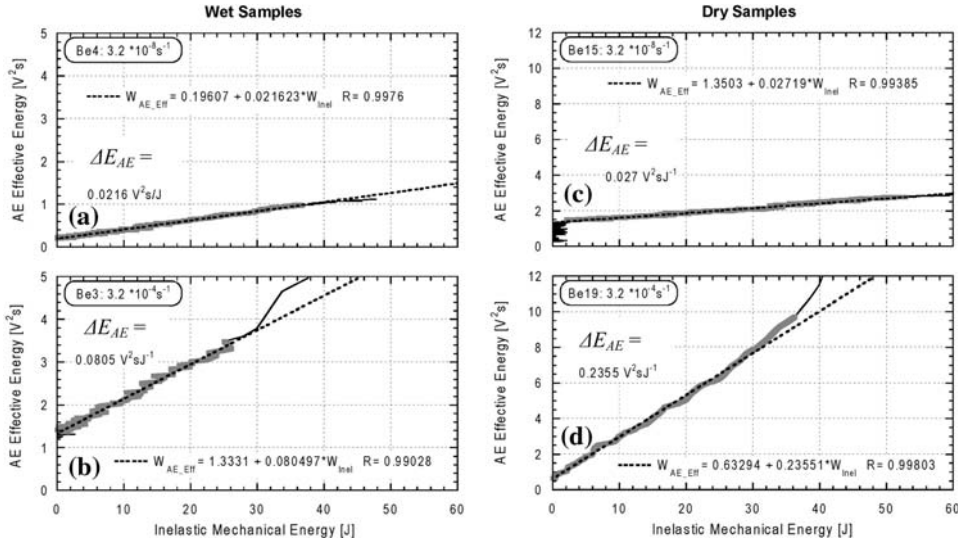
Figure 17
Effective radiated AE energy versus dissipated inelastic energy in wet (a), (b) and dry (c), (d) experiments
performed at slowest (a), (c) and fastest (b), (d) loading rates.

conditions and fast loading rates. At high loading rates unstable cracking is dominant.
This is in agreement with observations of BACKERS *et al.* (2005) on mode I fracturing of
sandstone. They found that increasing the loading rate by four orders of magnitude
resulted in a five-fold increase of AE events.

5. Conclusions

Nucleation of compaction bands in notched specimens is indicated by the appearance
of AE clusters close to the notch tips, a drastic increase of correlation coefficient
(*C* value), an increase in AE activity and the onset of inelastic deformation. With
progressive loading, AE activity increased and AE hypocenters indicated propagation of
a single CB normal to the sample axis. Completion of CB was indicated by maximum of
AE amplitudes and maximum AE activity, coinciding with AE hypocenter location near
the center of specimens and a decrease of P-wave velocities across the CB. Location of
CB and AE hypocenter locations shows excellent spatial agreement. Microstructural
analysis of deformed samples confirmed that regardless of the applied loading rate, the
reduced porosity inside the band ranges from 10–15%, while outside the band, the rock
matrix remains mostly undeformed with porosity of about 24%. We found slightly higher
mean width of CB in the fastest experiment Be3 ($H_{CB} = 0.92$ mm) in comparison with
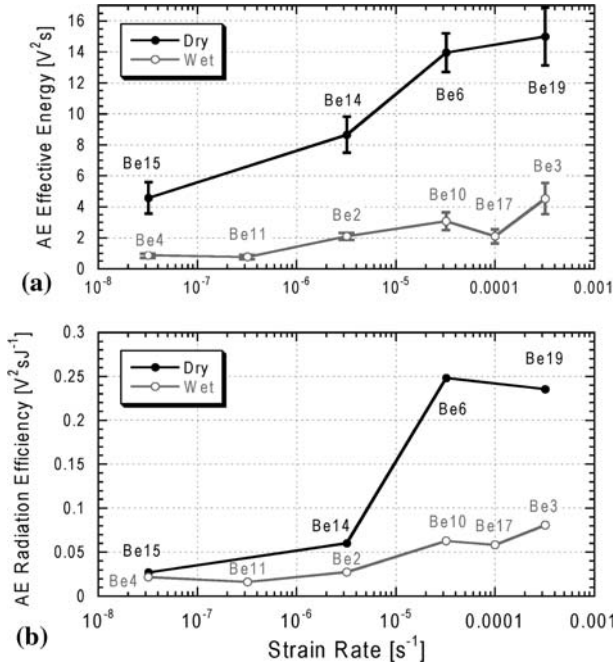the slowest experiment Be4 ($H_{CB} = 0.8$ mm), but both values are very close to the initial

Figure 18

Effective cumulative radiated AE energy at the moments of CB completion (a) and AE radiation efficiency (b) versus strain rate. Solid symbols — dry experiments, open symbols — wet experiments. Error bars correspond to the uncertainty of CB completion moments determination shown in Figure 13.

notch width. During propagation of CB pore volume reduction is linearly related to the area covered by AE hypocenters, and compactive shortening of the CB damage zone remains constant during CB propagation. Local porosity reduction inside the CB is about 10%–15% in agreement with microstructural observation. In all samples, lateral propagation of CBs was about 100 times faster than axial shortening rates. At the slowest displacement rate, AE activity during band propagation was reduced and CB nucleation in wet conditions occurred at 20% lower stresses. In both dry and wet samples, inelastic compaction energy per area ranged between 16 and 80 kJ m^{-2}, in good agreement with previous estimates from laboratory and field studies.

REFERENCES

ATKINSON, B.K. and MEREDITH, P.G (1981), *Stress corrosion of quartz: A note on the influence of chemical environment*, Tectonophysics *77*, 1–11.

ATKINSON, B.K. and MEREDITH, P.G., *Experimental fracture mechanics data for rocks and minerals*. in *Fracture Mechanics of Rock,* ed. B. K. Atkinson, pp. 477–525 (Academic Press, London. (1987)).

BACKERS, T., STANCHITS, S., and DRESEN, G. (2005), *Tensile fracture propagation and acoustic emission activity in sandstone: The effect of loading rate*, Int. J. Rock. Mech. Min. Sci. *42*, 7–8, 1094–1101.

BAUD, P. and MEREDITH, P.B. (1997), *Damage accumulation during triaxial creep of Darley Dale sandstone from pore volumometry and acoustic emission*, Int. J. Rock. Mech. Min. Sci. *34*, Art. 024.

BAUD, P., KLEIN, E., and WONG, T.-F. (2004), *Compaction localization in porous sandstones: Spatial evolution of damage and acoustic emission activity*, J. Struct. Geol. *26*, 603–624.

BAUD, P., VAJDOVA, V., and WONG, T.-F. (2006), *Shear-enhanced compaction and strain localization: Inelastic deformation and constitutive modeling of four porous sandstones*, J. Geophys. Res. 111, B12401, doi:10.1029/2005JB004101.

BORJA, R.I. and AYDIN, A., (2004), *Mathematical and geologic framework for failure modes in granular rocks*, Comput. Methods Appl. Mech. Eng. *193*, 2667–2698.

BRACE, W.F., PAULDING Jr. B.W., and SCHOLZ, C. (1966), *Dilatancy in the fracture of crystalline rocks*, J. Geophys. Res. *71*(16), 3939–3953.

COSTIN, L.S. (1983), *A microcrack model for the deformation and failure of brittle rock*, J. Geophys. Res. *88*(B11), 9485–9492.

DIGIOVANNI, A.A., FREDRICH, J.T., HOLCOMB, D.J., and OLSSON, W.A., *Micromechanics of compaction in an analogue reservoir sandstone*. In Girard, J., Liebman, M., Breeds, C., Doe, T. (eds.), Proc. *the North American Rock Mechanics Symposium*, July 31. (A.A. Balkema, Rotterdam, (2000)), pp 1153–1158.

EDMOND, J.M. and PATERSON, M.S. (1972), *Volume changes during the deformation of rocks at high pressures*. Int. J. Rock. Mech. Min. Sci. *9*, 161–182.

ESHELBY, J.D. (1957), *The determination of the elastic field of an ellipsoidal inclusion, and related problems*. Proc. Royal Society of London (A), *Mathematical and Physical Sciences 241* (1226), 376–396.

ISSEN, K.A. and RUDNICKI, J.W. (2000), *Conditions for compaction bands in porous rock*, J. Geophys. Res. *105*, 21529–21536.

FORTIN, J. SCHUBNEL, A., and GUEGUEN, Y. (2005), *Elastic wave velocities and permeability evolution during compaction of Bleurswiller sandstone*, Int. J. Rock. Mech. Min. Sci and Geomech. *42*, 873–889.

FORTIN J., STANCHITS S., DRESEN, G., and GUEGUEN, Y. (2006), *Acoustic emission and velocities associated with the formation of compaction bands in sandstone*, J. Geophys. Res. 111, B10203, doi:10.1029/2005JB003854.

FORTIN, J., STANCHITS, S., DRESEN, G., and GUEGUEN, Y. (2008), *Acoustic emissions monitoring during inelastic deformation of porous sandstone: Comparison of three modes of deformation*, Pure Appl. Geophys. this issue.

HAIMSON, B. (2001), *Fracture-like borehole breakouts in highporosity sandstone: are they caused by compaction bands?* Phys. Chem. Earth. A *26*, 15–20.

HAIMSON, B.C. (2003), *Borehole breakouts in Berea sandstone reveal a new fracture mechanism*, Pure Appl. Geophys. *160*, 813–831.

HAIMSON, B. and KOVACICH, J. (2003), *Borehole instability in highporosity berea sandstone and factors affecting dimensions and shape of fracture-like breakouts*, Eng. Geol. *69*, 219–23.

HAIMSON, B. and LEE, H. (2004), *Borehole breakouts and compaction bands in two high-porosity sandstones*, Int. J. Rock Mech. Min. Sci. *41*, 287–301.

HIRATA, T., SATOH, T., and ITO, K. (1987), *Fractal structure of spatial distribution of microcracking in rock*, Geophys. J. R. astr. Soc. *90*, 369–374.

KATSMAN, R. AHARONOV, E. and SCHER, H. (2006), *Localized compaction in rocks: Eshelby's inclusion and the Spring Network Model*, Geophys. Res. Lett. 33, L10311, doi:10.1029/2005GL025628.

KATSMAN, R. and AHARONOV, E. (2006), *A study of compaction bands originating from cracks, notches, and compacted defects*. J. Struct. Geol. *28*, 508–518.

KLAETSCH, A.R. and HAIMSON, B.C., *Porosity-dependent fracture-like breakouts in St. Peter sandstone*. In HAMMAH *et al.* (eds.), *Mining and tunneling innovation and opportunity* (University of Toronto Press, Toronto, (2002)) pp. 1365–1372.

KLEIN, E., BAUD, P., REUSCHLE, T., and WONG, T.-F. (2001), *Mechanical behaviour and failure mode of Bentheim sandstone under triaxial compression*, Phys Chem Earth (A) *26*, 21–25.

KLEIN, E. and REUSCHLÉ, T. (2003), *A model for the mechanical behaviour of bentheimsandstone in the brittle regime*, Pure Appl. Geophys. *160*, (5,6), 833–849.

LEI, X., NISHIZAWA, O., KUSUNOSE, K., and SATOH, T. (1992), *Fractal structure of the hypocenter distributions and focal mechanism solutions of acoustic emission in two granites of different grain sizes*. J. Phys. Earth. *40*, 617–634.

LEI, X., KUSUNOSE, K., RAO, M.V.M.S., NISHIZAWA, O., and SATOH, T. (2000), *Quasi-static fault growth and cracking in homogeneous brittle rock under triaxial compression using acoustic emission monitoring*. J. Geophys. Res. *105*, 6127–6139.

LEONARD, M. and KENNETT, B.L.N. (1999), *Multi-component autoregressive techniques for the analysis of seismograms*, Phys. Earth Planet. Int. *113* (1–4), 247.

LOCKNER, D.A., and BYERLEE, J.D. (1977), *Acoustic emission and creep in rock at high confining pressure and differential stress*, Bull. Seismol. Soc. Am. *67*, 247–258.

LOCKNER, D.A., BYERLEE, J.D., KUKSENKO, V., PONOMAREV, A. and SIDORIN, A. (1991), *Quasi-static fault growth and shear fracture energy in granite*, Nature *350*, 39–42.

LOCKNER, D.A., BYERLEE, J.D., KUKSENKO, V., PONOMAREV, A. and SIDORIN, A., *Observations of quasistatic fault growth from acoustic emissions*. In Fault Mechanics and Transport Properties of Rocks (Eds. B. Evans and T.-F. Wong), pp. 3–31 (Academic Press, London. (1992)).

LOCKNER, D.A. (1993), *The role of acoustic emission in the study of rock fracture*, Int. J. Rock Mech. Min. Sci. Geomech. *30*, 883–899.

MOLLEMA, P.N., and ANTONELLINI, M.A. (1996), *Compaction bands: A structural analog for anti-mode I cracks in Eolian sandstone*, Tectonophysics *267*, 209–228.

NELDER, J. and MEAD, R. (1965), *A simplex method for function minimisation*, Computer J. *7*, 308–312.

ODA, H., KOAMI, H. and SEYA, K. (1989), *Effect of occurrence rate of acoustic emissions on their statistical behaviour*. Pure Appl. Geophys. *130, 5–29.*

OLSSON, W. and HOLCOMB, D. (2000), *Compaction localization in porous rock*, Geophys. Res. Lett. *27*(21), 3537–3540.

A. REINICKE, A., STANCHITS, S., NAUMOV, D.J., LEGARTH, B.A., HUENGES, E. and DRESEN, G. (2008), *Mechanically Induced Permeability Reduction at the Fracture Proppant Interface*, Int. J. Rock Mech. Min. Sci. Geomech., submitted.

RUDNICKI, J.W. and STERNLOF, K. (2005) *Energy release model of compaction band propagation*. Geophys Res Lett. *32*, (L16303), doi:10.1029/2005GL023602.

RUDNICKI, J.W. (2007), *Models for compaction band propagation*, Geological Society, London, Special Publications 2007; v. *284*; pp. 107–125, doi:10.1144/SP284.8.

RUTTER, E.H. and MAINPRICE D.H. (1978), *The effect of water on stress relaxation of faulted and unfaulted sandstone*, Pure Appl. Geophys. *116*, 634–654.

SCHOLZ, C.H. (1968), *Microfracturing and the Inelastic Deformation of Rock in Compression*, J. Geophys. Res. *73*(4), 1417–1432.

STANCHITS, S., VINCIGUERRA, S., and DRESEN, G. (2006), *Ultrasonic Velocities, Acoustic Emission Characteristics and Crack Damage of Basalt and Granite*. Pure Appl. Geophys. *163* (5–6), 975–994, doi: 10.1007/s00024-006-0059-5.

STERNLOF, K.R., CHAPIN, J.R., POLLARD, D.D., and DURLOFSKY, L.J. (2004), *Permeability effects of deformation band arrays in sandstone*, AAPG Bull *88*, 1315–1329.

STERNLOF, K.R., RUDNICKI, J.W. and POLLARD, D.D. (2005), *Anticrack inclusion model for compaction bands in sandstone*, J. Geophys. Res. 110, B11403, doi:10.1029/2005JB003764.

STERNLOF, K.R., KARIMI-FARD, M., POLLARD, D.D., and DURLOFSKY, L.J. (2006), *Flow and transport effects of compaction bands in sandstone at scales relevant to aquifer and reservoir management*, Water Resour. Res. 42, W07425, doi:10.1029/2005WR004664.

TAYLOR, W.L., and POLLARD, D.D. (2000), *Estimation of in-situ permeability of deformation bands in porous sandstone, Valley of Fire, Nevada*, Water Resour. Res. *36*, 2595–2606.

TEMBE, S., VAJDOVA, V., WONG, T.-F., and ZHU, W. (2006), *Initiation and propagation of strain localization in circumferentially notched samples of two porous sandstones*. J. Geophys. Res. 111, B02409, doi:10.1029/2005JB003611.

THOMPSON, B.D., YOUNG, P. and LOCKNER, D. (2006), *Fracture in Westerly granite under AE feedback and constant strain rate loading: Nucleation, quasi-static propagation, and the transition to unstable fracture propagation*, Pure Appl. Geophys. *163*, 995–1019.

VAJDOVA, V. and WONG, T.-F. (2003), *Incremental propagation of discrete compaction bands: acoustic emission and microstructural observations on circumferentially notched samples of Bentheim sandstone*. Geophys. Res. Lett. 30(14), 1775, doi:10.1029/2003GL017750.

VAJDOVA, V., BAUD, P., and WONG, T.-F. (2004) *Permeability evolution during localized deformation in Bentheim sandstone*. J Geophys Res 109, B10406, doi:10.1029/2003JB002942.

WONG, T.-F. (1982), *Micromechanic of faulting in westerly granite*, Int. J. Rock Mech. Min. Sci. Geomech. Abstr. *19*, 49–64.

WONG, T.-F., BAUD, P., and KLEIN, E. (2001), *Localized failure modes in a compactant porous rock*. Geophys. Res. Lett. *28*, 2521–2524.

ZANG, A., WAGNER, F.C., and DRESEN, G. (1996), *Acoustic emission, microstructure, and damage model of dry and wet sandstone stressed to failure*, J. Geophys. Res. *101, 8, 17507–17521.*

ZANG, A., WAGNER, F.C., STANCHITS, S., DRESEN, G., ANDRESEN, R., and HAIDEKKER, M.A. (1998), *Source analysis of acoustic emissions in Aue granite cores under symmetric and asymmetric compressive loads*, Geophys. J. Internat. *135*, 1113–1130.

ZANG, A., WAGNER, F.C., STANCHITS, S., JANSSEN, C. and DRESEN, G. (2000), *Fracture process zone in granite*, J. Geophys. Res. *105*, 23651–23661.

To access this journal online:
www.birkhauser.ch/pageoph